Materials Advances

ROYAL SOCIETY OF CHEMISTRY

PAPER

View Article Online
View Journal | View Issue

Cite this: *Mater. Adv.*, 2026, 7, 1034

Exploring the influence of acceptor-strength in alkoxyphenanthrene-based A–π–D–π–A *versus* D–π–A architectures for resistive WORM memory devices

Senthilkumar V. Swetha,[a] Murali Ardra,[a] Predhanekar Mohamed Imran[b] and Samuthira Nagarajan *[a]

In the proliferation of resistive memory devices, organic small molecules play a vital role in high-density data storage technology. Effective tuning of organic molecules through strategic design enhances their memory characteristics. Herein, we present the first systematic investigation comparing symmetric A–π–D–π–A *versus* D–π–A-architected compounds, revealing fundamental structure–property relationships that govern the performance of memory devices. We synthesized a series of novel compounds featuring alkoxyphenanthrene as a central core donor moiety and an ethynyl spacer linking it with indoloquinoxaline/dibenzo[*a*,*c*]phenazine as the acceptor unit. All the synthesized compounds exhibited potent binary non-volatile WORM memory behavior with ON/OFF current ratios ranging from 10^3 to 10^4, long retention times of 2×10^3 s, and endurance characteristics of 100 cycles. Among the synthesized compounds, the A–π–D–π–A system attained a reduced threshold voltage of around −1.0 V over the other due to a well-balanced donor–acceptor system, leading to effective orbital overlap and charge distribution, a critical advancement over the D–π–A architecture device. The outperformance of the A–π–D–π–A systems was supported by the intramolecular charge transfer interactions and reduced energy band gap values observed in photophysical and electrochemical studies. The molecular simulations validated the efficient intramolecular charge transfer, which provides distinctive conductive states in the fabricated device, reinforcing the experimental observations. Thus, these insights suggest that the increase in acceptor strength in the system balances the push–pull interactions, aiming for a promising candidate for memory device applications.

Received 7th July 2025,
Accepted 23rd November 2025

DOI: 10.1039/d5ma00718f

rsc.li/materials-advances

Introduction

In this third decade of the twenty-first century, the development of high-density data storage devices is increasingly demanding innovative materials that combine efficient charge transport, stability, and scalability.[1–3] On the other hand, organic small molecules have emerged as a crucial class in electronic devices, fundamentally transforming their capabilities and applications as an alternative to inorganic semiconductor-based electronics.[4] Organic small molecules have gained prominence in this arena due to their modular structures, which allow precise tuning of electronic properties and straightforward synthetic routes.[5,6] Among these, donor–π–acceptor (D–π–A) systems have been extensively studied for their ability to facilitate intramolecular charge transfer, a key mechanism underpinning resistive switching behaviour in memory devices.[7] The electrical switching behaviour can be controlled by manipulating several key molecular design parameters.[8] These adjusting factors include the molecular design, the D–A configuration, the molecular planarity, the intrinsic strength of both the donor and acceptor units, and the nature of spacer linkages in the system.[9] Notably, Cann *et al.*[10] demonstrated how ethynyl spacers within the D–A architecture influenced memory performance. Along with molecular design and structure, there is a growing interest in exploring how various substituent electronic effects can modify the frontier molecular orbital levels, ultimately impacting the molecule's electronic band gaps.[11–14] Recent advances suggest that expanding this design to include dual acceptor units in an A–π–D–π–A architecture can further enhance the molecule's electronic interactions, leading to improved performance characteristics such as a high ON/OFF current ratio and lower operating voltages.[15–17] In this way, alkoxyphenanthrenes, as central core moieties end-capped with different terminal units, have already been explored and reported in OFET applications,

[a] *Department of Chemistry, Central University of Tamil Nadu, Thiruvarur, Tamil Nadu, India. E-mail: snagarajan@cutn.ac.in*
[b] *Department of Chemistry, Islamia College, Vaniampadi, India*

achieving a hole mobility of 0.85 $cm^2 V^{-1} s^{-1}$ with an ON/OFF current ratio of 10^8.[18] In general, phenanthrene derivatives provide a robust and planar π-conjugated donor core conducive to strong push–pull electronic interactions. The hexyloxy chains introduced at the 9 and 10 positions in phenanthrene will enhance solubility and improve humidity resistance.[18] In contrast, quinoxaline is a heterocyclic compound combining the pyrazine and benzene rings. Quinoxalines serve as outstanding electron-accepting units, mainly due to the strong electron-withdrawing effect of the two nitrogen atoms at the system's 1 and 4 positions.[19,20] These quinoxaline-based compounds have been extensively utilized to create highly optimized and customizable materials across various organic electronic applications.[21–24] A key benefit of incorporating quinoxaline as an acceptor lies in the ability to fine-tune the molecules' HOMO–LUMO energy gap by pairing it with different donor units, alongside the ease of modifying its molecular structure, given the multiple reactive sites available. Additionally, quinoxalines exhibit excellent ambient stability due to their inherently low HOMO energy levels. Polymers based on quinoxaline, functionalized with phenanthrene groups, have demonstrated exceptional memristor performance, achieving ON/OFF ratios exceeding 10^4. Shi and co-workers reported the development of two small quinoxaline-based organic molecules that displayed non-volatile WORM memory characteristics with ternary switching capabilities.[25] The inclusion of indole and phenanthrene units to the quinoxaline results in indoloquinoxaline and dibenzo[a,c]phenazine moieties, respectively. When functionalized with electron acceptors such as indoloquinoxaline and dibenzo[*a*,*c*]phenazine *via* ethynyl linkers, these molecules provide a versatile platform for investigating the effects of molecular architecture and intramolecular donor–acceptor interactions, as well as intermolecular donor–acceptor interactions on resistive memory functions.[26–29] In particular, it has been reported that the indoloquinoxaline moiety at the terminal end of the system provided exceptional behavior, transforming the device from SRAM to ternary WORM memory behavior.[30] Yu *et al.* have reported the synthesis of six donor–acceptor conjugated systems incorporating phenazine as the acceptor unit. They achieved high-performance multilevel memory storage, highlighting the strong electron-accepting ability of phenazine derivatives and their hierarchical charge-trapping nature.[31] Our research group has already explored the potential of the inbuilt D–A architectured indoloquinoxaline unit in memory device performance and found it to exhibit low threshold voltage and an ON/OFF ratio of 10^2.[32] It has been found that further tuning with suitable donors and modification in the designing strategy will make the indoloquinoxaline a potential candidate for memory device applications. Although the design and synthesis of numerous organic small molecules for resistive switching memory devices has been reported, it is worth noting that the architecture has primarily focused on either the D–π–A or A–π–D–π–A configuration.[33] Thus, focusing on the systematic analysis of head-to-head comparison of both architectures, we have designed the molecules to establish a structure–performance relationship in memory device applications.

In this work, we report the synthesis and comprehensive characterization of four novel organic small molecules featuring [3]-phenacene as the donor core combined with di- and monosubstituted acceptor units *via* acetylene bridges to form A–π–D–π–A and D–π–A systems, respectively. Through detailed studies of their UV-visible absorption, electrochemical behavior, thin film morphology, and resistive memory performance, established correlations were found between molecular structure and device metrics, including threshold voltage, endurance cycles, retention time, and ON/OFF current ratios. Complementary molecular simulations offer insight into intramolecular charge transfer efficiency and frontier orbital alignments, thereby reinforcing experimental observations. The primary objective behind this architectural manipulation is to explore and harness the potential of additional acceptors in the A–π–D–π–A architecture compared with the non-symmetrical D–π–A architecture.

Experimental section

Materials and methods

9,10-Phenanthroquinone, *N*-iodosuccinimide, trifluromethanesulfonic acid, 1-bromohexane, sodium dithionite, 5-bromoisatin, *o*-phenylenediamine, 4-bromo-1,2-phenylenediamine, 2-methylbut-3-yn-2-ol, potassium carbonate, Bu_4NBr, KOH, $Pd(PPh_3)_2Cl_2$, and copper iodide were used as purchased from commercial sources. ACS-grade solvents were used for spectroscopic analysis. Thin-layer chromatography was performed using silica gel A (F-254) precoated plates (0.25 mm) and visualized by UV irradiation. Silica gel with a particle size of 100–200 and 230–400 mesh was used for column chromatography to purify the compounds. A Bruker 400 MHz spectrometer was used to record ^{1}H NMR and ^{13}C NMR using tetramethylsilane (TMS) as the internal standard and $CDCl_3$ as the solvent. Absorption and emission spectral studies were recorded using a JASCO UV-NIR spectrophotometer and a PerkinElmer LS 55 spectrophotometer. The CHI electrochemical analyser was used for cyclic voltammetry analysis. The surface morphology of the thin films was examined using scanning electron microscopy (SEM) with VEGA3 and TESCAN diffractometer instruments. Thermogravimetric analysis (TGA) was conducted on PerkinElmer STA8000 (Simultaneous Thermal Analyzer) at a heating rate of 20 °C min^{-1} under a nitrogen atmosphere. All the fabricated devices were analysed for memory characteristics using a Keithley 4200A SCS semiconductor parameter analyser under ambient conditions.

Results and discussion

Synthesis

A–π–D–π–A and D–π–A architecture compounds were designed with phenanthrene as the core donor moiety (Fig. 1). To have a comprehensive comparative study and to analyse the objective of balancing acceptor strength on memory behaviour, two different acceptor units, indoloquinoxaline and dibenzo[*a*,*c*]-phenazine, have been encapsulated into the donor unit through an ethynyl spacer, which provides stability and rigidity to the

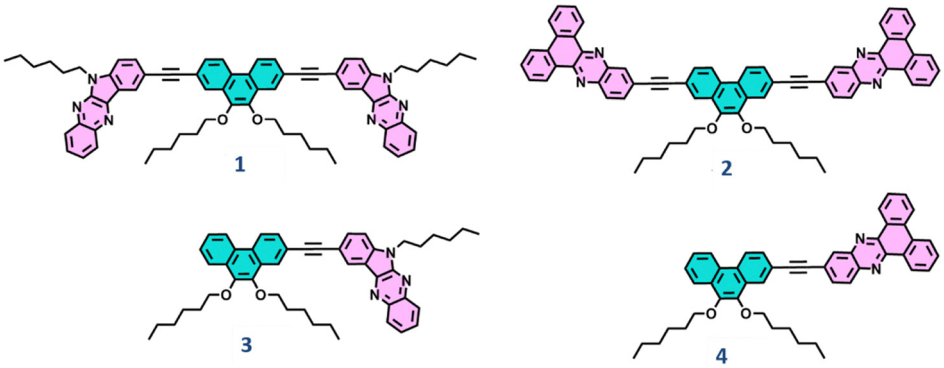

Fig. 1 Molecular structure of the compounds **1–4**.

molecular backbone (Schemes S1 and S2). The ethynyl linkage will also enhance π-delocalization in the system and optimize molecular planarity, which, conversely, facilitates tight, effective intermolecular stacking for efficient charge carrier transport.[34] The versatile nature of using organic compounds has been leveraged by utilizing phenanthrene-9,10-dione as a common precursor for synthesizing electron-donating and electron-accepting molecules. The strategic approach of using common precursors highlights the inherent tunability of organic compounds, allowing for systematic exploration of their electronic properties. 2,7-Diiodophenanthrene-9,10-dione and 2-iodophenanthrene-9,10-dione have been synthesized from phenanthrene-9,10-dione according to the reported literature synthetic procedure, with slight modifications.[18] Furthermore, the iodinated compounds have been reduced with $Na_2S_2O_4$ followed by hexylation using a phase transfer catalyst, Bu_4NBr, in a 1 : 1 THF and H_2O mixture. Introducing the "Lewis soft" oxygen atom to the system enhances the non-covalent interactions and pushes the electrons to the core moiety. The acceptor units indoloquinoxaline and dibenzo[*a*,*c*]-phenazine have been synthesized *via* a simple condensation reaction. The development of efficient synthetic routes enables the facile structural modification of shape-persistent acetylene derivatives using palladium-catalyzed coupling reactions. All synthesized compounds' structures were validated using ^{1}H NMR, ^{13}C NMR (Fig. S1–S11), and HR-MS spectroscopic techniques (Fig. S1–S15).

Photophysical properties

UV-vis absorption and emission spectra were recorded to understand the influence of additional acceptor units on the optical properties of the synthesized compounds. Fig. 2 illustrates the absorption and emission properties of the compounds **1–4** in 10^{-5} and 10^{-7} M dry tetrahydrofuran (THF) solution. Compounds substituting with the same acceptor group exhibited a similar absorption pattern in the range of near-UV (200 to 400 nm) owing to the delocalized π-system in the organic small molecules. Compounds with disubstituted acceptors **1** and **2** showed well-structured and stronger absorbance bands than their monosubstituted counterparts. This can be attributed to the increased π-conjugation provided by the additional acceptor in the system and the less twisted

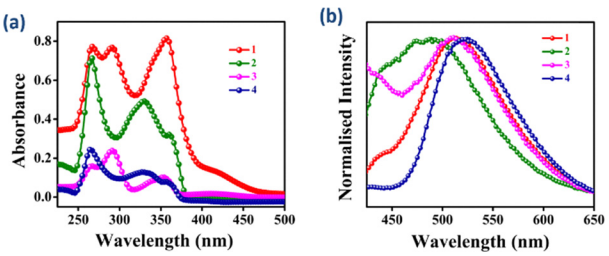

Fig. 2 (a) UV-vis absorption and (b) emission spectra of the compounds **1–4** in THF solution.

geometry resulting from the acetylene spacer. Under THF solution conditions, the synthesized compounds **1** and **3** exhibited two distinct high-energy absorption bands in the 250–300 nm range, attributed to their π–π* transitions.

A well-distinguished prominent peak in the 300–400 nm absorption band range can be ascribed to the n–π* transition arising from the heteroatoms in both the acceptor and donor units. Dibenzo[*a*,*c*]phenazine-substituted compounds **3–4** showed a bathochromic shift. This shift is likely due to the increasing acceptor strength compared to indoloquinoxaline-substituted compounds, as well as the enhanced acceptor unit modifications on the compounds' optical properties. The presence of the donor indole moiety in the molecular structure of indoloquinoxaline made it an inbuilt D–A system, decreasing its acceptor strength and resulting in a blue shift in the absorption maxima bands.

The weak absorption bands in the 375–500 nm wavelength range arise due to intramolecular charge transfer (ICT), resulting from charge transfer from the donor to the acceptor part of the molecule. For compounds **1** and **3**, a very weak absorption band centred around 415 to 430 nm, attributed to the ICT transition, has been observed.[35,36] This type of weaker absorption band for charge transfer has also been reported in fused donor–acceptor systems, such as thienopyrazines.[35] The compounds with disubstituted acceptor moieties **1–2** showed slight bathochromic shifts due to the extended π-conjugation and increased intramolecular acceptor strength.

The emission spectra were recorded at an excitation wavelength λ_{max}, determined from the absorption spectra of the corresponding compounds. The spectra were recorded at

Table 1 Photophysical properties of compounds **1–4**

Compounds	Experimental λ_{abs} (nm)	Experimental λ_{em} (nm)	Stokes shift (cm^{-1})	Absorption coefficient, ε (M^{-1} cm^{-1})
1	426, 356, 291, 267	513	8596	81 360
2	360, 329, 267	494	7534	70 942
3	417, 353, 292, 266	515	8911	23 821
4	359, 332, 264	522	8698	24 810

a concentration of 10^{-7} M in a THF solution. All the compounds exhibited emission maxima within the 410–472 nm range. Compared to A–π–D–π–A structured compounds, the D–π–A system showed a higher Stokes shift, attributed to their increased dipole moment arising from the molecular design (Table 1). Compound **3** showed a higher Stokes shift value among all the compounds due to its unsymmetrical molecular structure within the D–π–A architecture.

Electrochemical properties

Cyclic voltammetry was performed to gain a comprehensive understanding of the electrochemical properties and energy levels of the synthesized compounds. The cyclic voltammogram was recorded for the synthesized compounds on a three-electrode setup in a solution containing 0.1 mol L^{-1} tetrabutylammonium hexafluorophosphate (TBAPF6) in 10^{-3} M anhydrous *N*,*N*-dimethylformamide, with measurements taken at a scan rate of 100 mV s^{-1} (Fig. S17). The data obtained from the CV plot have been summarized in Table 2. Ferrocene was used as an external standard for calibrating the potential measurements, assuming that the absolute energy level is 4.8 eV with respect to the zero-vacuum level. From the onset of oxidation potential, the HOMO energy level value has been estimated. Furthermore, the LUMO energy level has been calculated from the difference between the HOMO and the energy band gap. This provides key insights into the electronic structure of the compounds.[37] All the compounds showed a sudden current drop in the range of 1.22–1.63 eV, indicating the irreversible oxidation process in the system. Due to more extended π-conjugation, A–π–D–π–A exhibited higher oxidation potential than compound **4**.[38]

Among all the compounds, dibenzo[*a*,*c*]phenazine substituted compound **4** distinguished itself by displaying the highest HOMO energy level value of −5.4 eV. In contrast, the remaining exhibited HOMO values in the range of −5.7 to −5.8 eV, indicating a relatively narrow and smaller difference range among them. The extended additional π-bridge and end acceptor groups have a significant impact on the optical bandgap. This lower bandgap further supports the enhanced charge carrier properties in compounds **1–2**. These findings demonstrate that introducing an additional acceptor unit to the system has a significant impact on its HOMO–LUMO energy levels. The low-lying HOMO levels offer substantial advantages not only for enhancing the stability of memory devices against oxygen-induced oxidation but also for facilitating efficient hole transfer from the ITO electrode, which is a critical process for device operation. Thus, the relatively low HOMO levels in compounds **1–2** are beneficial for achieving better performance in memory device applications.

Table 2 Electrochemical properties of compounds **1–4**

C. no.	Experimental E_{ox} (V)	Experimental E_{HOMO} (eV)	Experimental E_{LUMO} (eV)	Experimental E_g (eV)	Computational E_{HOMO} (eV)	Computational E_{LUMO} (eV)	Computational E_g (eV)
1	1.587	−5.806	−2.597	3.209	−5.083	−1.961	3.123
2	1.638	−5.853	−2.622	3.231	−5.211	−2.424	2.998
3	1.572	−5.793	−2.433	3.360	−5.422	−1.946	3.264
4	1.224	−5.447	−2.143	3.304	−5.475	−2.315	3.159

Morphological studies of thin films

The morphology and microstructure of thin films in the active layer have a crucial influence on the overall device performance. Thus, scanning electron microscopy (SEM) analysis was conducted to gain a deeper understanding of the thin film morphology of the active layers. The thin films of compounds **1–4** were prepared by depositing the compounds onto an ITO-coated glass substrate and then thermal annealing at 80 °C for 30–40 minutes. Fig. 3 displays the SEM images of thin films formed by the compounds **1–4**. Each compound formed a uniformly covered thin film, confirming their effective, organized molecular packing and the formation of a well-connected network.

This uniformity ensures enhanced charge transport capabilities. It is evident that compounds **1–4**, which substitute the same acceptor moieties, exhibit a dense network of fibre-like hierarchical topology. Apparently, a layered stacking pattern is observed for compound **2**, whereas compound **4** exhibits an

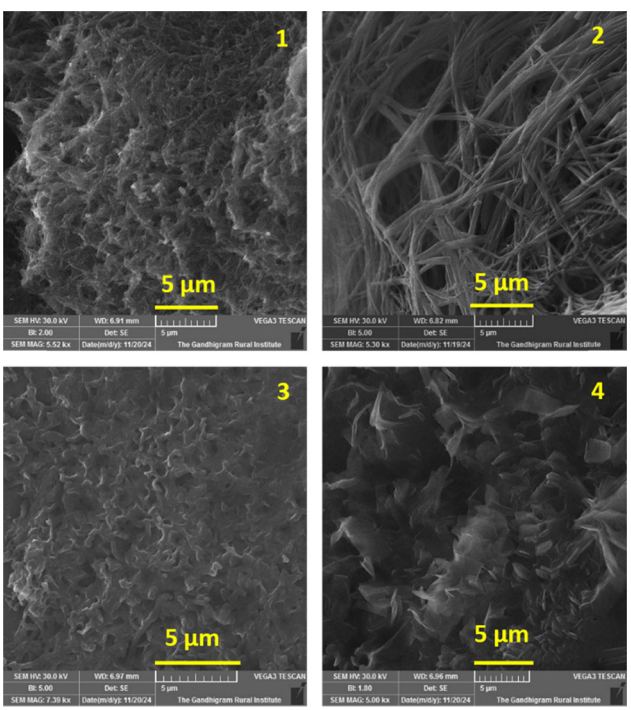

Fig. 3 SEM images of compounds **1–4**.

assembly of overlapping flakes within each layer. High-quality film formation facilitates seamless charge transport channels, reduces trap-induced scattering, and stabilizes resistive states, enhancing the endurance and retention of memory devices.

The crystallinity of thin films plays a crucial role in determining device performance. High crystallinity can facilitate more efficient charge transport by providing well-ordered molecular packing and reducing disordered orientation within the film.

To investigate the structural order of the fabricated thin films, X-ray diffraction (XRD) measurements were recorded (Fig. S16). Compounds **1** and **3** displayed sharp diffraction peaks at 11.74°, 19.69°, and 24.65°, corresponding to *d*-spacings of 7.53, 4.50, and 3.60 Å. On the other hand, compounds **2** and **4** exhibited diffraction peaks that differed from each other, indicating distinct structural arrangements. Specifically, compound **2** exhibited sharp diffraction peaks at 17.99°, 19.34°, 25.08°, and 32.70°, corresponding to *d*-spacings of 4.93, 4.58, 3.54, and 2.73 Å, respectively. Multiple, sharp diffraction peaks with small *d*-spacing values correspond to a highly ordered, semi-crystalline structure and efficient molecular packing in the film.[39]

The crystallite sizes of all the compounds are found to be in the range of 27 to 32 nm. The crystallite size and the *d*-spacing values of the compounds are summarised in Table S1. It is to be noted that the A–π–D–π–A structured compounds have been observed with a slight decrement in crystallite size compared to that of the D–π–A structured compounds. This could be due to the well-ordered packing system by the extended π-conjugation in the di-substituted compounds. The enhanced molecular stacking and crystallinity are particularly significant as they contribute to the formation of effective pathways for charge carrier transport within the material. The thin film XRD results further confirm the absence of significant structural defects or irregularities in the film, which could otherwise hinder charge transport and negatively impact device performance.

The surface of the fabricated thin film should be uniform and make smooth interfaces to provide favourable and sustained interfacial contact with the electrodes. Thus, the surface morphology has also been analysed using the Atomic Force Microscope (AFM) technique by coating the thin film of the compound over a silicon substrate. The recorded AFM image of compounds **1–4** is depicted in Fig. 5, along with the corresponding height profile. The thin film surface of all the compounds is found to exhibit a root mean square (RMS) roughness value ranging from 2 to 7 nm. Compounds **2** and **4**, which have the same acceptor units, showed RMS values of 6.12 and 5.29 nm, respectively. In comparison, compounds **1** and **3**, with indoloquinoxaline as the acceptor unit, showed lower RMS values of 2.32 and 2.78 nm, respectively.

This low RMS roughness value indicates the effective prevention of Ag nanoparticle diffusion into the film. The smooth interfaces help to maintain the film's integrity and prevent performance degradation caused by metallic infiltration. Furthermore, a reduced roughness at the interface significantly lowers the charge carrier injection barrier between electrodes and the active layer. Consequently, the improved charge injection, coupled with the prevention of nanoparticle diffusion, collectively enhances the overall charge carrier migration within the film, leading to improved device efficiency and stability.

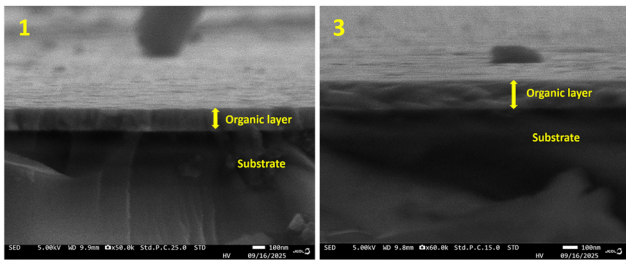

Fig. 4 FE-SEM cross-sectional image of the thin-film coated with compounds **1** and **3**.

To get more insight into the thickness and homogeneity of the thin film, FESEM cross-sectional analysis of the thin film for representative compounds **1** and **3** was carried out (Fig. 4). It shows well-defined and uniform coating of the active layer over the substrate, with thickness values in the range of 200–300 nm. The obtained thickness range is deemed beneficial for memory device performance.

Thermal stability

To investigate the decomposition temperature and overall thermal resilience of the synthesized compounds, thermogravimetric analysis (TGA) was conducted under a nitrogen atmosphere. The samples were subjected to a consistent heating rate of 20 °C min^{-1}, allowing for precise observation of weight changes as a function of temperature.

Although the compounds contain alkyl units, all of them exhibited good thermal stability, with a decomposition temperature (T_d, 5% weight loss) of over 380 °C in a nitrogen atmosphere (Fig. 6). This indicates their robustness under elevated temperatures. Compared to indoloquinoxaline-substituted compounds **1** and **3**, dibenzo[*a*,*c*] phenazine-substituted compounds **2** and **4** showed a considerable char yield of approximately 30%. This variation can be attributed to the increased number of alkyl units in the acceptor units added to the system in compounds **1** and **3**. The high decomposition temperature indicates the compounds' stability during the device fabrication process and exhibits operational stability at a considerable temperature range.

Memory characteristics

The resistive switching memory behaviour of the synthesized compounds was studied using current–voltage (*I*–*V*) measurements.

These measurements were performed on sandwich-type devices, configured as ITO/**1–4**/Ag, under an applied voltage sweep, and the findings are illustrated in Fig. 7. During the recordings, the devices were monitored using an incrementing voltage sweep in 0.1 V steps, where the top Ag electrode was biased, and the bottom ITO electrode was grounded. All the devices coated with compounds **1–4** as active layers demonstrated clear resistive switching properties. Initially, the devices exhibited a low conductivity (OFF) state, but a sudden and

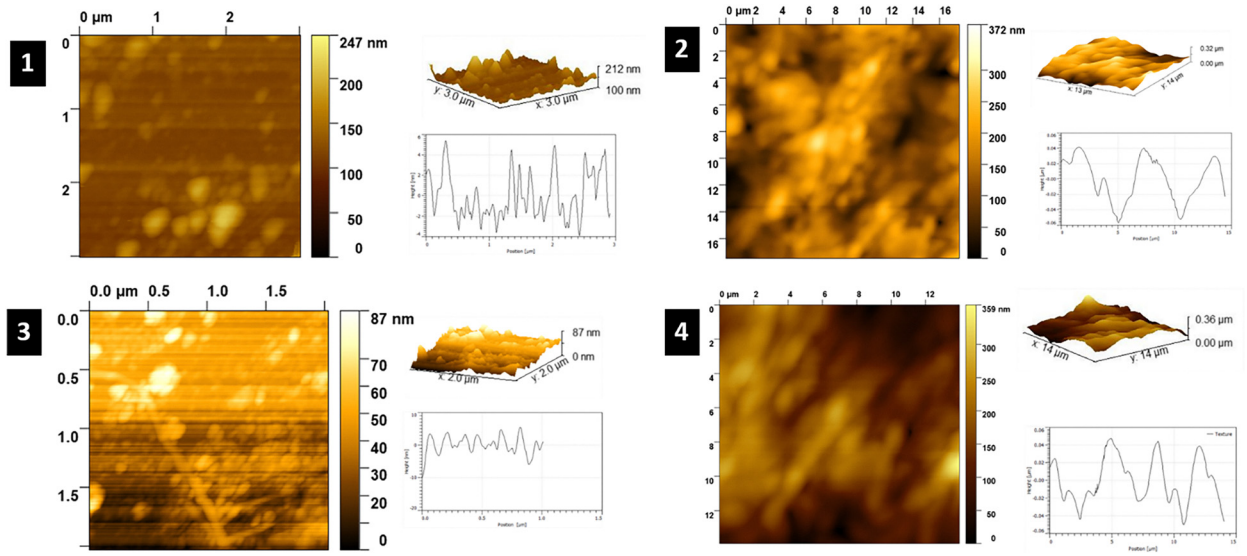

Fig. 5 AFM images of the compounds **1–4** with their corresponding height profile and 3D image of the surface.

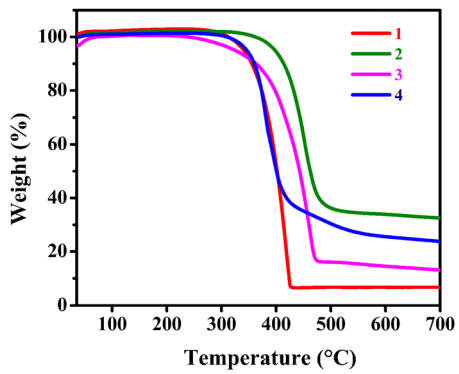

Fig. 6 Thermogravimetric analysis (TGA) plot of the compounds **1–4** with a heating rate of 20 °C min^{-1} under an inert atmosphere.

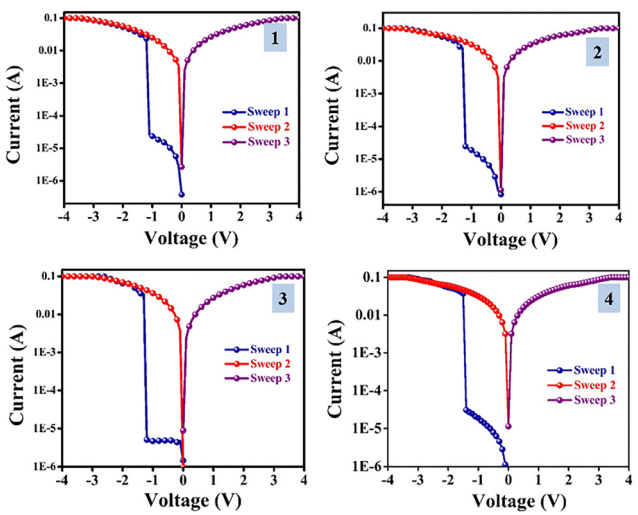

Fig. 7 Current–voltage (*I–V*) characteristics of the A–π–D–π–A-based devices (ITO/**1–2**/Ag) and D–π–A-based devices (ITO/**3–4**/Ag).

Table 3 Memory device parameters of compounds **1–4**

Compounds	ON/OFF current ratio[a]	Threshold voltage[a] (V)
1	10^3	−1.04 ± 0.10
2	10^4	−1.02 ± 0.17
3	10^4	−1.21 ± 0.08
4	10^3	−1.41 ± 0.06

[a] Calculated from the mean of 20 cells.

abrupt increase in current was observed upon applying a negative voltage sweep from 0 to −4 V (sweep 1). This serrated transition represents the point at which the device shifts from a low-conductivity (OFF) state to a high-conductivity (ON) state at a defined threshold voltage, ranging from −1.02 to −1.41 V (Table 3). This abrupt transition from a high-resistance state (HRS) to a low-resistance state (LRS) signifies the ''writing'' operation in digital memory applications. During the second scanning cycle, the voltage is swept from 0 to −4 V (sweep 2). At this point, the device is in an LRS state, with the current maintaining the stability.

This phase can be considered the ''reading'' operation for the stored data. The device maintained its ON state during a subsequent voltage sweep in a positive direction from 0 to 4 V (sweep 3), corresponding to the reading process. Once the device is turned ON, it maintains its LRS state even when the electric field is removed. This certainly means that the switching process from HRS to LRS is not reversible even in the absence of an electrical power supply, which signifies the non-volatile nature of the device.

Consequently, the devices displayed stable and well-defined non-volatile binary WORM memory behaviour, with distinct ON/OFF current ratios ranging from 10^3 to 10^4. Compounds **1** and **2** exhibited a low threshold voltage, attributed to their planar nature, and provided continuous, seamless charge

transfer due to the presence of additional ethyl linkers and acceptors. This, in turn, reduces the charge injection barrier from the ITO to the HOMO of the system.

These findings indicate that devices featuring an A–π–D–π–A architecture exhibit enhanced electrical switching performance compared to their D–π–A counterparts. The incorporation of additional acceptor units strengthens the push–pull interactions within the system, thereby improving the overall memory device characteristics.

Compounds **1** and **3** exhibited a higher ON/OFF current ratio of 10^4, attributed to the favorable molecular packing and strong D–A interaction. The larger spatial separation between the HOMO and LUMO in the case of compound **3** reduces the overlap between the frontier orbitals, suppresses charge recombination, and stabilizes the charge-transfer state, thereby enhancing the high-resistance (OFF) state. This resulted in a higher ON/OFF ratio of 10^4 among all the compounds.

For commercialization, the stability and long-term use of the fabricated device are essential. Thus, the data retention features were investigated. The retention of the high and low conductivity states was tracked by applying a constant stress voltage of −0.5 V over 4000 seconds, during which no noticeable degradation occurred (Fig. 8).

In addition to evaluating data retention characteristics, the endurance cycle was examined to determine the number of times that the data can be processed from the device. Endurance cycle was assessed through repeated consecutive read cycles, where once the device is powered on, the LRS is continuously monitored at 1s intervals using the corresponding threshold voltage as the read voltage (Fig. 8). One hundred read operations were continuously carried out, revealing that the devices could reliably toggle between HR and LR states while maintaining consistent performance.

Only minimal, negligible distortion has been noted in the memory window over 100 cycles, indicating the device's stability. This impressive retention and endurance are attributed to the highly conjugated system and strong hole-transporting properties of the phenanthrene unit, which enhance device stability.[11]

The double logarithmic plot, $\log I$ *vs.* $\log V$, was plotted and interpreted using different conduction models to gain a more comprehensive understanding of the underlying mechanism of memory-switching,[40] including ohmic conduction and space-charge limited current (SCLC), as illustrated in Fig. 9. A distinct ohmic conduction in the OFF state is observed for all the compounds. A conduction transition is obtained when the device is subjected to a higher voltage bias. Specifically for compound 2, the conduction shifted from ohmic behaviour ($I \propto V$) to a trap-filled SCLC regime characterized by Child's square law ($I \propto V^2$), reflected by an increased slope of approximately 1.76. Interestingly, as the device transitioned to the ON state under higher bias, the conduction mechanism reverted to ohmic conduction, with the slope returning near 1. This observed switching behaviour is attributed to the applied voltage exceeding the specific threshold voltage, which is sufficient to overcome the energy barrier. This facilitates the filling of charge traps associated with electron-withdrawing moieties, enabling the device to transition into the ON state.[41]

For any fabricated device to be employed for commercial purposes, reproducible results for a statistically significant number of devices are essential. In this way, it has been observed that almost all the fabricated devices exhibit resistive switching, with slight variations in the memory window and threshold voltage. The threshold voltage for the switching process has varied slightly within certain ranges for 20 devices. The range of the threshold voltage is evident in the cumulative probability distributions shown in Fig. 10. Thus, device-to-device variability in the switching behavior has been analyzed using 20 different memory units and found to yield consistent results. All the cells exhibited reliable binary WORM memory behavior with a significant memory window varying from 10^3 to 10^5. Meanwhile, most of the fabricated cells showed an ON/OFF current ratio of 10^4. This indicates that the fabricated device can produce significant, reliable data suitable for WORM memory applications.

Proposed mechanism of memory behaviour

Molecular simulations were conducted to investigate the electronic properties and switching mechanisms of the compounds

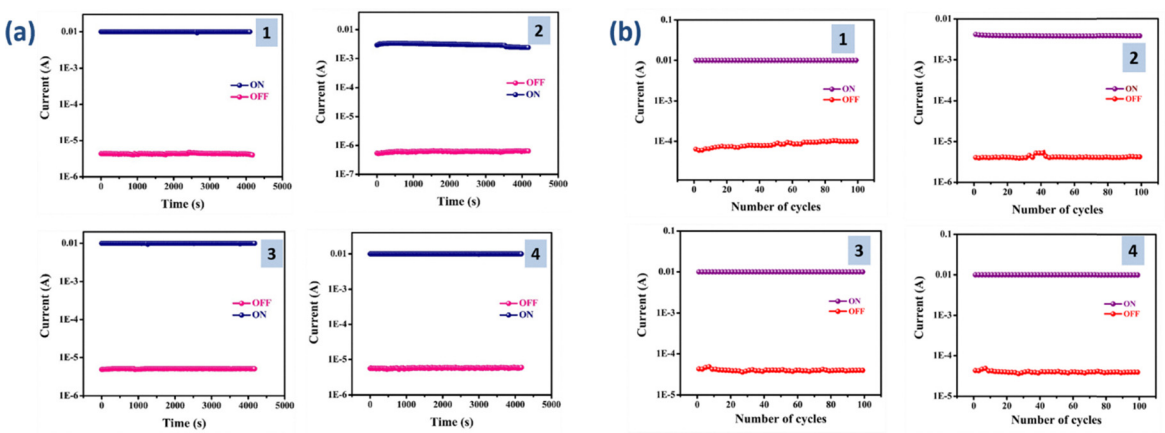

Fig. 8 (a) The retention characteristics and (b) the endurance cycle test of the fabricated devices (ITO/**1–4**/Ag).

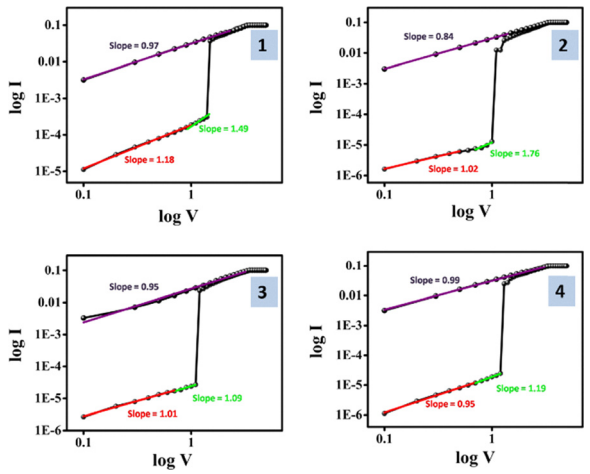

Fig. 9 Double logarithmic plot and corresponding linear fitting curve of the devices (ITO/**1–4**/Ag) in negative sweep.

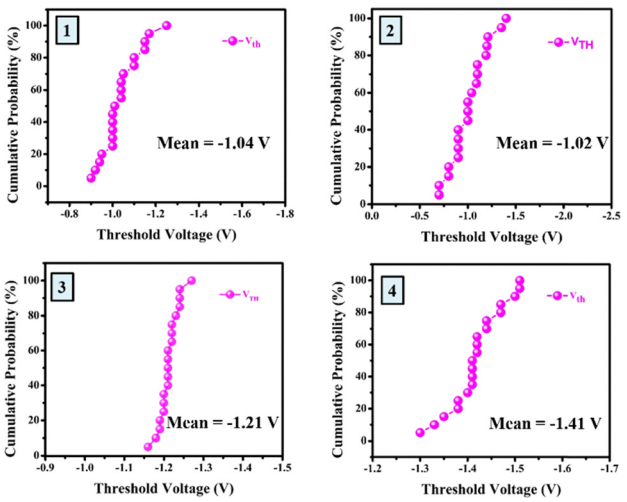

Fig. 10 Cumulative probability distributions *vs.* threshold voltage V_{th} in negative bias for the device ITO/**1–4**/Ag.

under study. A series of computational simulations, including molecular mechanics and semi-empirical methods, were used to determine the plausible stereochemistry of the structure, as it is an essential aspect for packing and predicting the molecular electronic properties of the system, some of which are typically non-covalent. These optimal geometrical parameters were then used to compute the optimized structure at the DFT's B3LYP level of theory and time-dependent density functional theory (TD-SCF) for spectral estimation theoretically using Gaussian. The optimized geometry for compounds **1–4** is shown in Fig. S19. The optimized geometry was then used as the input geometry for density of states (DOS) calculations using VASP (MedeA) software. However, the structures were evaluated using solvent correction parameters such as GGA-PBE (basis set), and the DOS graphs were subsequently obtained (Fig. S18). Density functional theory (DFT) computations were performed using GAUSSIAN-09 software and the 6-31G (d) level of basis set theory. This approach enabled the examination of electronic transitions and the assessment of the compounds' optical characteristics, offering a deeper understanding of their potential performance in electronic applications. A detailed quantitative study of the orbitals involved in transition with symmetry-labelled levels is possible, but will be beyond the scope of this article. This kind of transition has been considered a characteristic of good charge transport.

Based on DFT calculations of the HOMO and LUMO energy levels, compounds **1–2** exhibited comparatively elevated HOMO values, reduced LUMO levels, and optimal band gap energies. These FMOs are further validated by the electronic transitions predicted through TDDFT analysis (Table S2–S4). Fig. 12 illustrates the summarized molecular orbital energy levels of the compounds. Thus, all the compounds exhibited memory characteristics by facilitating resistive switching behaviour supported by ICT from the HOMO, primarily located on the central core donor moiety alkoxy-attached phenanthrene unit, to the LUMO, which is situated on the acceptor units in the terminal segments. Quinoxaline and phenazine units in the acceptor units attached to the donor phenacene core serve as effective electron-trapping centres. This configuration in the system facilitates optimized charge separation and efficient charge transfer from the core donor phenanthrene unit (HOMO) to the peripheral acceptor sites (LUMO), resulting in the formation of charge-transfer complexes. In compounds **2** and **4**, the molecular architecture featuring phenazine units positioned at the terminal ends is an effective electron acceptor. At the same time, the phenacene moiety occupies the central position, functioning as a donor unit. This resulted in a significant increase in charge density within the central phenacene unit in the HOMO level. Following this transfer, the generated holes create conductive pathways that cause a sudden increase in current, enabling the device to transition from an OFF state to an ON state.[9,42–44]

Furthermore, to analyse the switching mechanism observed in the sandwich devices ITO/**1–4**/Ag, the HOMO and LUMO energy levels of the compounds were compared against the work functions of ITO and Ag, as depicted in Fig. 11. The comparison

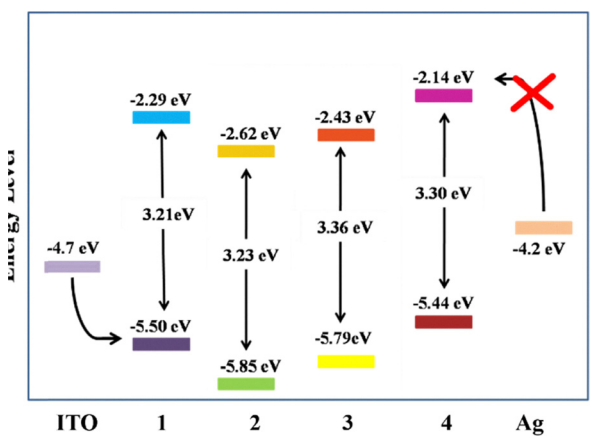

Fig. 11 Energy levels of compounds **1–4** along with the work function of electrodes.

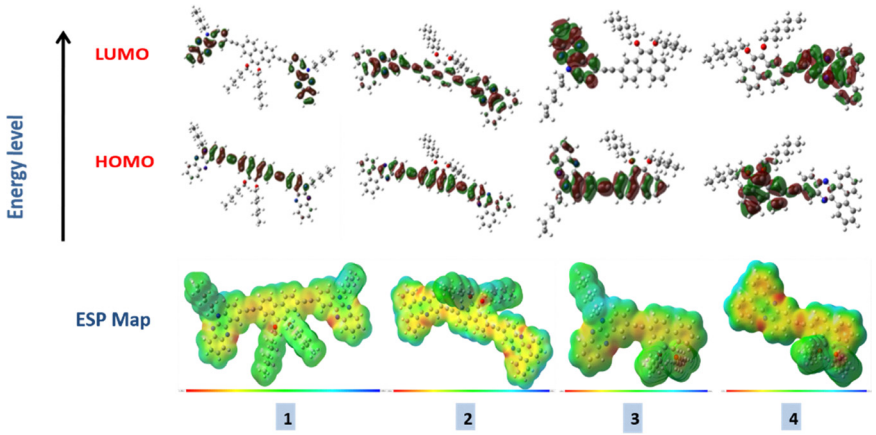

Fig. 12 HOMO and LUMO energy levels and ESP map of the compounds **1–4**.

revealed that the minimal energy barrier between the ITO work function and the HOMO energy level facilitates the efficient hole injection from ITO into the HOMO, which is energetically favourable, making it the preferred charge injection pathway. The charge injection barrier analysis between the ITO and HOMO level of the compound is compared with the charge injection barrier between the Ag and LUMO level. From this, it can be noted that the preferred pathway for hole injection from ITO to the HOMO energy level is more viable than the electron injection from Ag to the LUMO level due to the lower charge injection barrier. The latter path is characterized by a significantly higher energy barrier, making it less energetically favourable. Understanding these energy relationships is crucial for optimizing the performance and switching behavior of these devices.[45,46]

To gain deeper insight into the switching behavior, the electrostatic potential (ESP) diagram was analyzed to investigate the relationship between charge distribution and memory performance (Fig. 12). The ESP visualization displays a color gradient shift from blue to red, indicating a progressive reduction in electron density. A persistent, mild negative red region is observed over the alkoxy chain in the central moiety, which can be attributed to the lone pairs of electrons on the oxygen atoms. These electron-rich regions appear as densely packed lobes, reflecting localized electron density. A red region is observed in the quinoxaline and phenazine moieties, arising from the lone pair of nitrogen atoms in the system. The blue area in the alkyl chain in the system can serve as an open pathway for charge carriers, facilitating their movement along the molecular framework and providing intermolecular interactions. In contrast, the electron-withdrawing quinoxaline unit in all the molecules has been depicted in the red region. Thus, in all cases, the terminal unit acts as the charge trap in the presence of a quinoxaline unit.[47]

Conclusions

To summarize, a series of novel A–π–D–π–A and D–π–A based molecules with phenacene as the donor unit, and two different terminal acceptor subunits, indoloquinoxaline and dibenzo[*a*,*c*]phenazine, were synthesized. This study systematically explored the influence of donor and acceptor units, with a particular focus on the significance of the extended π–A framework and the impact of varying acceptor strengths on the memory performance of organic small-molecule-based non-volatile memory devices. In particular, the relevance of the D–π–A framework and how varying acceptor strengths affect the memory characteristics in organic small molecule-based non-volatile memory devices were determined. The photophysical investigations have strongly supported the findings, revealing the compounds' ICT behavior. All the compounds exhibited absorption maxima in the 353–360 nm range. An irreversible anodic peak is observed between 1.2 and 1.6 V, confirming the oxidation of the donor moiety. Introducing an additional acceptor unit in the A–π–D–π–A architecture reduces the energy gap compared to the monosubstituted D–π–A system. Additionally, the morphological studies of the thin films revealed uniform coverage for all compounds, indicating their strong ability to support efficient charge carrier transport. Each compound exhibited binary non-volatile WORM memory behavior, with an ON/OFF current ratios ranging from 10^3 to 10^4, stable retention times of up to 2000 s, and consistent endurance over 100 cycles. Notably, compounds featuring disubstituted acceptor units achieved the lowest threshold voltages, approximately −1.0 V. The superior performance of the A–π–D–π–A systems is linked to a reduced hole injection barrier and narrower HOMO–LUMO band gaps. Molecular simulation studies further corroborate the presence of effective intramolecular charge transfer, which is responsible for the distinct conductive states observed in the devices. Collectively, the results highlight the potential of phenacene-based A–π–D–π–A-architectured compounds, which, upon further tuning, can serve as promising candidates for next-generation organic resistive memory device applications, advancing the pursuit of efficient, stable, and scalable non-volatile data storage devices.

Author contributions

Swetha, S. V: design, synthesis, methodology, data curation, data interpretation, and writing – original draft; Ardra, M: writing,

review and editing; Predhanekar M. Imran: computational analysis; Nagarajan, S: design, supervision, review and editing. The manuscript was written with contributions from all authors. All authors have approved the final version of the manuscript.

Conflicts of interest

There are no conflicts to declare.

Data availability

The data supporting this article have been included as part of the supplementary information (SI). Supplementary information provides synthetic routes, ^{1}H. ^{13}C NMR, and HR-MS spectral data, thin film analysis, cyclic voltammogram, computational studies, and memory device fabrication of the compounds **1–4**. See DOI: https://doi.org/10.1039/d5ma00718f.

Acknowledgements

The authors thank the Science & Engineering Research Board (SERB), New Delhi, for funding (CRG/2023/005788). The DST-FIST (SR/FST/CS-1/2021/215) and the Department of Chemistry, Central University of Tamil Nadu, India, are acknowledged for providing the necessary research facilities.

References

1 M. Malik, M. Henini, F. Ezema, E. Manikandan, J. Kennedy, K. Bouziane, M. Chaker, A. Gibaud, A. K. F. Haque, Z. Nuru, I. Ahmad, R. Obodo and M. Akbari, Peculiar Size Effects in Nanoscaled Systems, *Nanoscale Horiz.*, 2022, **1**, 1–36.

2 M. Pagliaro and J. M. Nedelec, Hybrid Materials, *Nanoscale*, 2014, **6**, 6219.

3 Z. Xue, J. Wang, X. Li, L. Mao, S. Tao, Z. Li, Z. Luo, S. Dai, N. Jiang, Z. Gan and Z. Ning, Highly Improved Shape Memory Properties of a PCL-Based Polyurethane via Polylactide Stereocomplexation, *ACS Appl. Mater. Interfaces*, 2025, **17**, 28704–28715.

4 V. M. Angela, D. Harshini, P. M. Imran and S. Nagarajan, Strategical Design and Synthesis of D–A–D-Based Quinolines for Improved WORM Memory, *J. Mater. Chem. C*, 2022, **11**, 1103–1110.

5 B. Cho, S. Song, Y. Ji, T. W. Kim and T. Lee, Organic Resistive Memory Devices: Performance Enhancement, Integration, and Advanced Architectures, *Adv. Funct. Mater.*, 2011, **21**, 2806–2829.

6 M. Akshaya, D. Harshini, R. Gayathri, P. M. Imran and S. Nagarajan, Asymmetrically Functionalized Phenanthro-[9,10-*d*]Imidazole-Based Donor-Acceptor Architectures for High-Performance Ternary Memory Devices, *ACS Appl. Electron. Mater*, 2024, **6**, 7522–7539.

7 B. Dey, S. Sarkar, H. Banik and S. Arshad Hussain, Resistive Switching Behaviour of Organic Molecules, *Mater. Today Proc.*, 2019, **46**, 6290–6294.

8 X. Liu, H. Lian, L. Zhao, Z. Qin, T. Xiao, X. Jiang, T. Guan, S. Wang, P. Müller-Buschbaum and Q. Dong, Engineering Conjugated Bridges in TPE-BT-Based Donor-Acceptor Molecules for Optimized Resistive Random Access Memory, *ACS Appl. Mater. Interfaces*, 2025, **17**, 28459–28471.

9 H. C. Wu, J. Zhang, Z. Bo and W. C. Chen, Well-Defined Star-Shaped Donor-Acceptor Conjugated Molecules for Organic Resistive Memory Devices, *Chem. Commun.*, 2015, **51**, 14179–14182.

10 J. Cann, S. Dayneko, J. P. Sun, A. D. Hendsbee, I. G. Hill and G. C. Welch, N-Annulated Perylene Diimide Dimers: Acetylene Linkers as a Strategy for Controlling Structural Conformation and the Impact on Physical, Electronic, Optical and Photovoltaic Properties, *J. Mater. Chem. C*, 2017, **5**, 2074–2083.

11 J. Han, H. Lian, X. Cheng, Q. Dong, Y. Qu and W. Wong, Study of Electronic and Steric Effects of Different Substituents in Donor–Acceptor Molecules on Multilevel Organic Memory Data Storage Performance, *Adv. Electron. Mater.*, 2021, **7**, 2001097.

12 B. Y. Ma, X. Cao, G. Li, Y. Wen, Y. Yang, J. Wang, S. Du, L. Yang, H. Gao and Y. Song, Improving the ON/OFF Ratio and Reversibility of Recording by Rational Structural Arrangement of Donor – Acceptor Molecules, *Adv. Funct. Mater.*, 2010, **20**, 803–810.

13 E. Wang, M. Pan, Y. Chen, H. Zeng, W. Duan and H. Huang, Multistate Polarization and Enhanced Nonreciprocal Transport in Two-Dimensional van der Waals Ferroelectric Heterostructures, *Nano Lett.*, 2025, **25**, 8843–8850.

14 C. Yang, H. Wang, K. Wang, Z. Cao, F. Ren, G. Zhou, Y. Chen and B. Sun, Silk Fibroin-Based Biomemristors for Bionic Artificial Intelligence Robot Applications, *ACS Nano*, 2025, **19**, 17173–17198.

15 I. Salaoru and S. Paul, Memory Devices Based on Small Organic Molecules Donor-Acceptor System, *Thin Solid Films*, 2010, **519**, 559–562.

16 Q. Bao, H. Li, Y. Li, J. He, Q. Xu, N. Li, D. Chen, L. Wang and J. Lu, Comparison of Two Strategies to Improve Organic Ternary Memory Performance: 3-Hexylthiophene Linkage and Fluorine Substitution, *Dyes Pigm.*, 2016, **130**, 306–313.

17 R. K. Canjeevaram Balasubramanyam, R. Kumar, S. J. Ippolito, S. K. Bhargava, S. R. Periasamy, R. Narayan and P. Basak, Quadrupolar (A–π–D–π–A) Tetra-Aryl 1,4-Dihydropyrrolo[3,2-*b*]Pyrroles as Single Molecular Resistive Memory Devices: Substituent Triggered Amphoteric Redox Performance and Electrical Bistability, *J. Phys. Chem. C*, 2016, **120**, 11313–11323.

18 B. Balambiga, P. Devibala, P. M. Imran and S. Nagarajan, Tunable Charge Transport Using Heterocycles-Flanked Alkoxyphenanthrenes for High-Performing OFETs, *ACS Omega*, 2024, **9**, 42091–42102.

19 C. Zhang, Y. Li, Y. Zhou, Q. Zhang, H. Li and J. Lu, Deriving Highly Oriented Organic Nanofibers and Ternary Memory

Performance: Via Salification-Induced Effects, *Chem. Commun.*, 2018, **54**, 10610–10613.
20 J. Waluk and E. W. Thulstrup, Excited States of Indoloquinoxalines, *Spectrochim. Acta, Part A*, 1988, **44**, 1335–1340.
21 A. J. Payne, J. S. J. McCahill and G. C. Welch, Indoloquinoxaline as a Terminal Building Block for the Construction of π-Conjugated Small Molecules Relevant to Organic Electronics, *Dyes Pigm.*, 2015, **123**, 139–146.
22 D. Kanekar, S. S. Dhanawade, A. B. Jadhav, M. Ghadiyali and S. Chacko, Fluorescent Indolo[2,3-*b*]quinoxalin-2-yl)(Phenyl)-Methanone Dyes: Photophysical, Aie Activity, Electrochemical, and Theoretical Studies, Research Square, 2021, 1–23.
23 R. M. Kamble, B. K. Sharma, A. M. Shaikh and S. Chacko, Design, Synthesis, Opto–Electrochemical and Theoretical Investigation of Novel Indolo[2,3-*b*]Naphtho[2,3-*f*]Quinoxaline Derivatives for n-Type Materials in Organic Electronics, *ChemistrySelect*, 2018, **3**, 6907–6915.
24 D. N. Kanekar, S. Chacko and R. M. Kamble, Quinoxaline Based Amines as Blue-Orange Emitters: Effect of Modulating Donor System on Optoelectrochemical and Theoretical Properties, *Dyes Pigm.*, 2019, **167**, 36–50.
25 E. Shi, H. Zhuang, Z. Liu, X. Cheng, H. Hu, N. Li, D. Chen, Q. Xu, J. He, H. Li, J. Lu and J. Zheng, Two Quinoxaline Derivatives Designed from Isomer Chemistry for Nonvolatile Ternary Memory Device Applications, *Dyes Pigm.*, 2015, **122**, 66–73.
26 C. Wang, J. Wang, P. Z. Li, J. Gao, S. Y. Tan, W. W. Xiong, B. Hu, P. S. Lee, Y. Zhao and Q. Zhang, Synthesis, Characterization, and Non-Volatile Memory Device Application of an n-Substituted Heteroacene, *Chem. - Asian J.*, 2014, **9**, 779–783.
27 C. Wang, M. Yamashita, B. Hu, Y. Zhou, J. Wang, J. Wu, F. Huo, P. S. Lee, N. Aratani, H. Yamada and Q. Zhang, Synthesis, Characterization, and Memory Performance of Two Phenazine/Triphenylamine-Based Organic Small Molecules through Donor-Acceptor Design, *Asian J. Org. Chem.*, 2015, **4**, 646–651.
28 A. M. Shaikh, B. K. Sharma, S. Chacko and R. M. Kamble, Novel Electroluminescent Donor-Acceptors Based on Dibenzo[*a,c*]Phenazine as Hole-Transporting Materials for Organic Electronics, *New J. Chem.*, 2017, **41**, 628–638.
29 F. M. Xie, H. Z. Li, G. L. Dai, Y. Q. Li, T. Cheng, M. Xie, J. X. Tang and X. Zhao, Rational Molecular Design of Dibenzo[*a,c*]Phenazine-Based Thermally Activated Delayed Fluorescence Emitters for Orange-Red OLEDs with EQE up to 22.0%, *ACS Appl. Mater. Interfaces*, 2019, **11**, 26144–26151.
30 D. Harshini, V. M. Angela, P. Devibala, P. M. Imran, N. S. P. Bhuvanesh and S. Nagarajan, Improved Resistive Switching WORM Memory Behavior in D-π-A Architectures by Modifying the Terminal Donor Units, *ACS Appl. Electron. Mater.*, 2022, **4**, 4383–4395.
31 H. Yu, Y. Du, J. Li, S. Zhao, C. Wang, S. Wang and H. Chang, Ternary Memory Devices Based on Copolymers of Dipyrido-[3,2-*a*:2′,3′-*c*]Phenazine Acceptor and Multiple Donors, *ACS Appl. Polym. Mater.*, 2024, **6**, 9453–9465.
32 S. V. Swetha, R. Gayathri, M. Ardra, P. M. Imran and S. Nagarajan, Inherent D–A Architecture in Indoloquinoxalines with an Array of Substituents for Non-Volatile Memory Device Applications, *ChemPhysChem*, 2024, **25**, 202400003.
33 X. Wang, H. Lian, L. Zhao, Z. Qin, Y. Yang, T. Xiao, S. Wang and Q. Dong, Tailoring Memory Performance via Engineering Conjugated Bridges in Benzo[*c*][1,2,5]Thiadiazole Based Donor–Acceptor Small Molecules, *Chem. Phys. Mater.*, 2025, **4**, 360–371.
34 N. P. Redmore, I. V. Rubtsov and M. J. Therien, Synthesis, Electronic Structure, and Electron Transfer Dynamics of (Aryl)Ethynyl-Bridged Donor-Acceptor Systems, *J. Am. Chem. Soc.*, 2003, **125**, 8769–8778.
35 P. Tyagi, A. Venkateswararao and K. R. J. Thomas, Solution Processable Indoloquinoxaline Derivatives Containing Bulky Polyaromatic Hydrocarbons: Synthesis, Optical Spectra, and Electroluminescence, *J. Org. Chem.*, 2011, **76**, 4571–4581.
36 Y. Chen, Y. Ling, L. Ding, C. Xiang and G. Zhou, Quinoxaline-Based Cross-Conjugated Luminophores: Charge Transfer, Piezofluorochromic, and Sensing Properties, *J. Mater. Chem. C*, 2016, **4**, 1–3.
37 K. J. Rountree, B. D. Mccarthy, E. S. Rountree, T. T. Eisenhart and J. L. Dempsey, A Practical Beginner's Guide to Cyclic Voltammetry, *J. Chem. Educ.*, 2017, **95**, 197–206.
38 P. Blanchard, C. Malacrida, C. Cabanetos, J. Roncali and S. Ludwigs, Triphenylamine and Some of Its Derivatives as Versatile Building Blocks for Organic Electronic Applications, *Polym. Int.*, 2019, **68**, 589–606.
39 H. Hu, J. He, H. Zhuang, E. Shi, H. Li, N. Li, D. Chen, Q. Xu, J. Lu and L. Wang, Single Atom Substitution to Alter the Molecular, *J. Mater. Chem. C*, 2015, **3**, 8605–8611.
40 B. Sun, X. Li, T. Feng, S. Cai, T. Chen, C. Zhu, J. Zhang, D. Wang and Y. Liu, Resistive Switching Memory Performance of Two-Dimensional Polyimide Covalent Organic Framework Films, *ACS Appl. Mater. Interfaces*, 2020, **12**, 51837–81845.
41 Y. Qi, Z. Shen, C. Zhao and C. Zhou, Effect of Electrode Area on Resistive Switching Behavior in Translucent Solution-Processed AlO x Based Memory Device, *J. Alloys Compd.*, 2020, **822**, 153603.
42 F. Chen, G. Tian, L. Shi, S. Qi and D. Wu, Nonvolatile Write-Once Read-Many-Times Memory Device Based on an Aromatic Hyperbranched Polyimide Bearing Triphenylamine Moieties, *RSC Adv.*, 2012, **2**, 12879–12885.
43 C. Wang, M. Yamashita, B. Hu, Y. Zhou and J. Wang, Synthesis, Characterization, and Memory Performance of Two Phenazine/Triphenylamine-Based Organic Small Molecules through Donor-Acceptor Design, *Asian J. Org. Chem.*, 2015, **4**, 646–651.
44 N. Rajan, I. Maity, S. Saikh and A. K. Mukherjee, A Low-Voltage Solution-Processed Organic Small Molecule Memristor Based on TIPS Pentacene, *ACS Appl. Electron. Mater.*, 2025, **7**, 779–787.
45 J. H. Li, Y. Li, J. T. Xu and C. K. Luscombe, Self-Assembled Amphiphilic Block Copolymers/CdTe Nanocrystals for Efficient Aqueous-Processed Hybrid Solar Cells, *ACS Appl. Mater. Interfaces*, 2017, **9**, 17942–17948.

46 M. U. Khan, G. Hassan and J. Bae, Non-Volatile Resistive Switching Based on Zirconium Dioxide: Poly (4-Vinylphenol) Nano-Composite, *Appl. Phys. A: Mater. Sci. Process.*, 2019, **125**, 1–11.

47 Q. Zhang, J. He, H. Li, N. Li, Q. Xu, D. Chen and J. Lu, A Novel Ternary Memory Property Achieved through Rational Introduction of End-Capping Naphthalimide Acceptors, *J. Mater. Chem. C*, 2017, **5**, 7961–7968.